ADVANCED FUNCTIONAL MATERIALS
www.afm-journal.de

Freestanding Graphitic Carbon Nitride Photonic Crystals for Enhanced Photocatalysis

Lu Sun, Meijia Yang, Jianfeng Huang, Dingshan Yu, Wei Hong, and Xudong Chen**

Graphitic carbon nitride (g-C_3N_4) has attracted tremendous attention in photocatalysis due to its extraordinary features, such as good thermal and chemical stability, metal-free composition, and easy preparation. However, the photocatalytic performance of g-C_3N_4 is still restricted by the limited surface area, inefficient visible light absorption, and high recombination rate of photoinduced charge carriers. Herein, a facile synthesis to produce freestanding g-C_3N_4 photonic crystals (PCs) by crack-free, highly ordered colloid crystals templating is reported. The PC structure succeeded from the silica opals induces bicontinuous framework, stronger optical absorption, and increase in the lifetime of photoexcited charge carriers compared to that of the bulk g-C_3N_4, while the chemical structure remains similar to that of the bulk g-C_3N_4. As such, the g-C_3N_4 PCs have a much higher photodegradation kinetic of methyl orange and photocatalytic hydrogen production rate which is nearly nine times the rate of bulk g-C_3N_4.

1. Introduction

Photocatalytic technology applied in water purification and hydrogen evolution has attracted a great research interest as it provides potential solution to severe environment pollution and sustainable energy.[1] Recently, a stable and eco-friendly semiconductor-based photocatalyst with a suitable band gap of ≈2.7 eV, graphite-carbon nitride (g-C_3N_4), was found to show photocatalytic performance under visible light.[2] Nevertheless, the inherent deficiency of this material, including low specific surface area, inefficient use of the visible light, and a high recombination rate of electron/hole, limited its practical application.[1a,3] Great effort has been made for improving the photocatalytic activity of g-C_3N_4 by chemical modification and nanostructure regulation.[3–21] Chemical modification based on crystalline and molecular engineering could turn the band gap of g-C_3N_4 by element doping,[4] using different precursors,[5–9] introducing crystal defects or amorphous structure,[3,10,11] forming carbon vacancies,[12] fabricating heterojunction composites,[13–15] and so on. Structural regulation mainly focused on increasing specific surface area,[16–21] typically making mesoporous by templates with high specific surface area.[16,17,20,21] However, most of studies reported focused on g-C_3N_4 in the powder form due to the contradiction between the highly open framework and the insufficient mechanical strength. Some recent progresses have been made to achieve 3D macroform g-C_3N_4 based on robust substrate,[19] but major challenges remain to develop a substrate-free g-C_3N_4 film with high photocatalytic activity.

Photonic crystals (PCs) are materials with spatially periodic variation of the dielectric permittivity on the order of the wavelength of light. The propagation of light within a certain frequency range is forbidden in a certain crystal direction within a certain spectrum regime, namely photonic stopband.[22,23] Special properties of PCs, such as inhibition of spontaneous emission,[24–26] slow light, and amplified photon absorption/emission,[27–30] provide numerous possibilities for "photon management" applications. Thus introducing PC structure is a promising strategy for promoting photocatalytic activity of photocatalyst and the performance in optoelectronic devices.[27–33] Consequently, if g-C_3N_4 is fabricated in a PC form, the spontaneous emission by the recombination of photogenerated carriers could be inhibited and the photocatalytic activity could benefit from the bicontinous network with increased visible light absorption via slow photon effects.

Inspired by considerations above, herein we demonstrate a general solution approach to tackle the challenge via a freestanding colloidal crystal templating method (see **Scheme 1**). Freestanding, highly ordered, crack-free silica PCs are generated by evaporative-vertical deposition. Subsequently, the calcination of the precursor dicyandiamide (DCDA) followed by removal of silica PCs generates highly uniform macroscopic g-C_3N_4 PC films. The resultant freestanding g-C_3N_4 PCs possesses a 3D interconnected network with tunable photonic stop band, exhibiting significantly improved photocatalytic activity in photodegrading and water splitting under visible light.

L. Sun, M. Yang, Prof. D. Yu, Dr. W. Hong, Prof. X. Chen
Key Laboratory for Polymeric Composite and Functional Materials of Ministry of Education
School of Chemistry and Chemical Engineering
Sun Yat-sen University
Guangzhou 510275, P.R. China
E-mail: hongwei9@mail.sysu.edu.cn; cescxd@mail.sysu.edu.cn
J. Huang
School of Chemistry and Chemical Engineering
Sun Yat-sen University
Guangzhou 510275, P.R. China

DOI: 10.1002/adfm.201600894

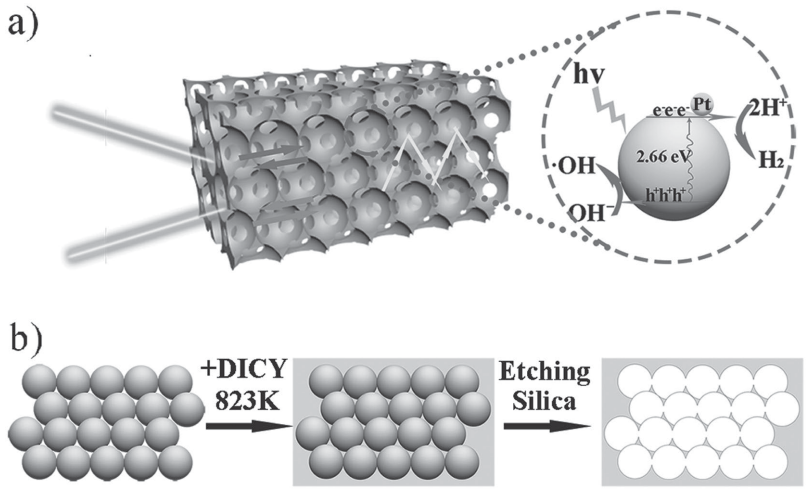

Scheme 1. Schematic illustrations for a) the g-C_3N_4 PCs in photocatalysis and b) the preparing route to obtain g-C_3N_4 PCs.

2. Results and Discussion

2.1. Microstructure and Stop Band of Freestanding Silica PCs

Conventional self-assembly processes such as sedimentation,[34] shear flow,[35] spin-coating,[36] evaporative,[37] and "flowcontrolled" deposition have been widely used to fabricate colloidal crystal films with a typical single domain area of 20 μm (see Figure S1, Supporting Information),[38] but the yield and crystallinity of PCs were unsatisfactory because substantial precipitates and cracks formed during the self-assembly processes.[34–38] By controlling the evaporative deposition conditions, the silica PCs in this work had centimeter-scale single domain area, stop band full-width-at-half-maxima (FWHM) of 30 nm, with little wasteful sediment during the assembly. Figure S2 in the Supporting Information shows the scanning electron microscopic (SEM) images of 200 nm diameter silica PCs with scale bar of 100 μm, indicating that the PCs were highly ordered and regularly aligned in a large area with a thickness over 50 μm (Figure S2e, Supporting Information). The uniform reflected colors from the PCs, which were caused by Bragg diffraction of visible light, as observed in Figure S3a in the Supporting Information. The measured reflectance spectra for the PCs with different microsphere diameters along the PC ⟨111⟩ direction were shown in Figure S3b in the Supporting Information. These reflectance peaks were attributed to the stop-bands along the Γ–L direction in the reciprocal space of the PCs.[39] For comparison, disordered silica aggregate was fabricated via multi-dispersed microspheres under the same conditions as the silica PCs (see Figure S4 in the Supporting Information).

2.2. Microstructure and Stop Band of g-C_3N_4 PCs

The bulk g-C_3N_4, g-C_3N_4 inverse opals fabricated from the silica PCs and disordered silica aggregate were denoted as bulk-C_3N_4, 180-C_3N_4, 200-C_3N_4, 215-C_3N_4, 236-C_3N_4, 260-C_3N_4, and dis-C_3N_4, respectively. As shown in **Figure 1**, the spherical pores in the g-C_3N_4 PCs were 3D ordered with periodic macroporous structures. In addition, the macroporous structure was mechanical stable through powder grinding and photocatalysis reaction (see Figure S5, Supporting Information). The macropore sizes of the g-C_3N_4 PCs were found to be very close to the original colloidal sphere because of the hard templating.

The stop-bands of these g-C_3N_4 PCs in water were confirmed by the structural colors and the reflection spectra in **Figure 2**. The reflectance maxima of g-C_3N_4 PCs along the PC ⟨111⟩ direction in water red shifted about 40 nm compared to the original silica PCs templates in air because of the high refractive index of g-C_3N_4 (calculated as 1.8) and filling medium of water. For comparison, the reflectance spectra for bulk-C_3N_4 and dis-C_3N_4 with the same testing condition were shown in Figure S6 in the Supporting Information. As Figure S6 in the Supporting Information shows, no significant reflectance characteristic was detected, indicating that though there were many previous works using silica for templating carbon nitride,[16–18,20,21] the stop-bands in g-C_3N_4 could only achieved by highly ordered silica PC with sphere diameter about 200 nm.

More detailed information about the ordered and disordered framework of 200-C_3N_4 and dis-C_3N_4 was accessed by nitrogen absorption–desorption isotherms (see **Figure 3** and **Table 1**). Dis-C_3N_4 and 200-C_3N_4 were very similar in the distribution of micropores and mesopores. However, dis-C_3N_4 possessed higher specific surface area (57.6917 $m^2\ g^{-1}$) and correspondingly larger pore volume (0.3478 $cm^3\ g^{-1}$) than that of 200-C_3N_4

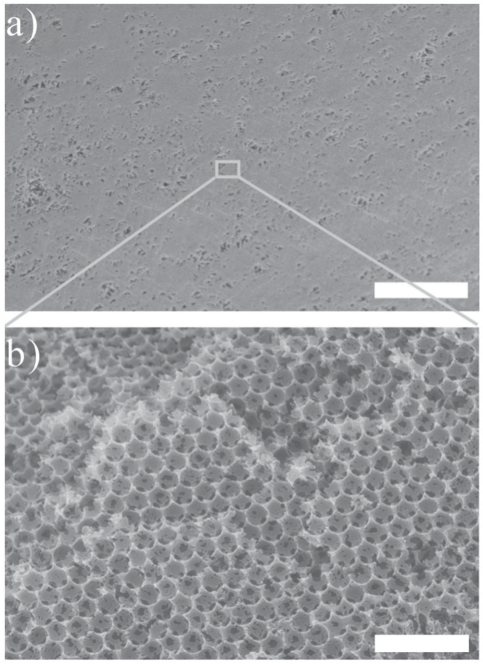

Figure 1. SEM images of the 200-C_3N_4. a) scale bar: 30 μm, b) scale bar: 1 μm.

DOI: 10.1002/adfm.201600894

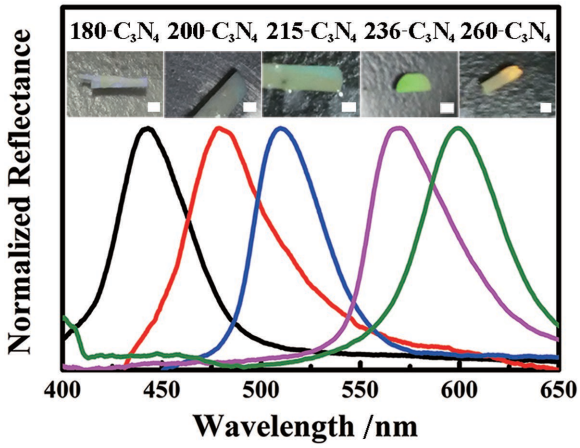

Figure 2. The reflectance spectra and the corresponding structural colors of the g-C_3N_4 PCs along the PC ⟨111⟩ direction in water. Scale bar: 1 mm.

(50.0022 and 0.2122 m^2 g^{-1}), because smaller microspheres could promote the surface area more effectively.

2.3. The Crystal and Chemical Structure States of g-C_3N_4 PCs

Direct evidence for the formation of g-C_3N_4 was obtained using X-ray diffraction (XRD), X-Ray photoelectron spectrometer (XPS), and elemental analysis.

As shown in **Figure 4**, the characteristic XRD patterns of the g-C_3N_4 PCs were similar to that of the bulk material. The diffraction peak at 27.6° was attributed to the {002} reflection of the conjugated aromatic stacking structure with a spacing about 0.32 nm, whereas the peak at 13.1° corresponded to the {001} reflection from the in-plane repeating unites of the continuous heptazine framework.[2]

In **Figure 5**, XPS measurements showed that two major carbon species and three nitrogen species existed in our products, including the sp^3-bonded carbon in C–C (≈284.6 eV) and N–C=N (≈288.2 eV), the sp^2-bonded nitrogen in C–N=C (≈398.6 eV), the nitrogen in tertiary N–$(C)_3$ groups (≈399.6 eV), and the presence of amino groups (C–N–H, ≈401.1 eV) caused by imperfect polymerization. No obvious binding energy shift of C 1s and N 1s core electrons was observed, suggesting that the chemical states of both carbon and nitrogen in the g-C_3N_4 PCs were the same as in the bulk g-C_3N_4.

The C/N ratios of different samples measured by elemental analysis are given in Table S1 in the Supporting Information, indicating that the C/N ratios of the g-C_3N_4 PCs were in accordance with the C/N ratio of bulk-C_3N_4.

The results above resembled the reference bulk-C_3N_4, suggesting that the g-C_3N_4 PCs were successfully fabricated via the melting-infiltration colloidal crystal templating method.

2.4. Band Structures and Photophysical Behaviors of Charge Carriers in g-C_3N_4 PCs

To characterize the process of charge separation and the energy-wasteful recombination in the g-C_3N_4 products, photoluminescence (PL) spectra and PL lifetime of the powdered g-C_3N_4 products (see **Figure 6**) were recorded as water suspensions, in accordance with the photocatalytic conditions. A strong PL emission was observed for the bulk-C_3N_4, due to the radiative recombination of charge carriers. The PL emission suppressed for dis-C_3N_4 sample, indicating that the bicontinuous framework could create large surface area for charge traps.[3,16] The PL emission was further suppressed for 200-C_3N_4, in spite of the lower specific surface area (see Table 1). Normalized PL spectra showed the obvious redshift of the PL emission due to the suppression below the PL maximum wavelength caused by the PCs with higher incident angle (see **Figure 7**). The PL emission of 200-C_3N_4 film in Figure S7 in the Supporting Information showed further redshift from that of the powder form, which supported the conclusion of PL suppression by the photonic stop band.

In addition, the lifetime of PL became longer due to the stop band suppression, in accordance with other studies where direction-dependent suppression of PL by PCs was observed with changes in PL lifetimes by about 10%.[40,41] When the stop band overlapped with the PL emission, the PL intensity would be suppressed, leading to energy transfer and the slower decay of the PL.[24–26,40,41] The hallmark feature of the PC structure was the decrease of photonic density of states when the stop band overlapped with the emission curve,[24,25,42] leading to suppressed exciton transition rates which lengthened the PL lifetime.[24,42] The photonic density of states in the g-C_3N_4 could

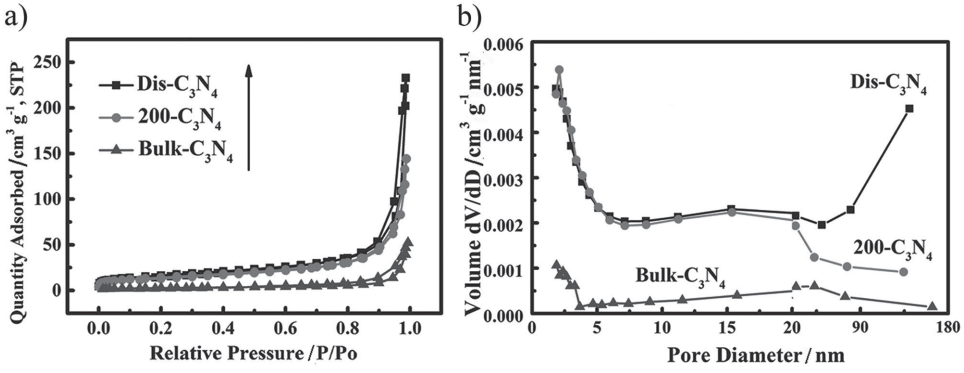

Figure 3. a) N_2 adsorption–desorption isotherms and b) BJH pore-size distributions for bulk-C_3N_4, dis-C_3N_4 and 200-C_3N_4, respectively.

Table 1. BET surface area and pore volume of g-C_3N_4 samples.

Sample	BET surface area [$m^2\ g^{-1}$]	Pore volume [$cm^{-3}\ g^{-1}$]
bulk-C_3N_4	9.4459	0.0803
Dis-C_3N_4	57.6917	0.3478
200-C_3N_4	50.0022	0.2122

dominate the transition probability from the excited state to the ground state during which the fluorescent photons generated, according to the Fermi's golden rule[43]

$$W = 2\pi\hbar|V_{fi}|^2\,\rho(E_{fi}) \quad (1)$$

where W is the transition rate, $\hbar$ is the reduced Planck constant, V_{fi} is the matrix element of the potential that operates between the initial and final value, $\rho(E_{fi})$ is the density of states at the energy of the transition. Consequently, the suppressed transition rates of the exciton meant suppressed radiative combination, leading to weaker PL intensity and improving the probability of exitons' (namely charge carriers') involvement in photocatalytic reactions before recombination.

The electronic band structure of the 200-C_3N_4 was investigated by a combined analysis of UV–vis diffuse reflectance spectrum (DRS) and the Mott–Schottky plots. UV–vis diffuse reflectance spectrum of 200-C_3N_4 featured a typical semiconductor-like absorption (see **Figure 8**) with a band edge at ≈460 nm corresponding to 2.66 eV. A remarkably enhanced light-harvesting ability within a wide range of visible light for the 200-C_3N_4 over the bulk-C_3N_4 was considered as a result of multiple scattering and the slow photon effects within the structure. Stronger reflectance by the stop band was also observed in the UV–vis DRS (see Figure S8 in the Supporting Information). However, the corresponding semiconductor bandgap energy and conduction band (CB) determined by electrochemical Mott–Schottky plots (see Figure S10 in the Supporting Information) for the 200-C_3N_4 had no significant change from that of the bulk-C_3N_4.

The increased UV–vis absorption was also reflected in the increased photocurrent. The electron-transfer conductivity confirmed by the photocurrent (Figure S9, Supporting Information) for 200-C_3N_4 was consistent with the increased UV–vis absorption in Figure 8, indicating the improved charge separation, hence an enhancement of the photocatalytic performance.

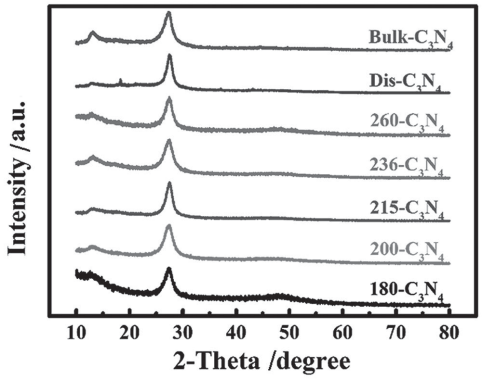

Figure 4. Powder XRD patterns of the g-C_3N_4 samples.

2.5. Improved Photocatalytic Activities of g-C_3N_4 PCs

In order to demonstrate the PC structure–function correction of the g-C_3N_4 PCs, we evaluated the photodegradation of methyl orange (MO) in **Figure 9**a and H_2 evolution activity (HER) in Figure 9b under visible light irradiation ($\lambda > 420$ nm).

No detectable degradation of MO was measured under the visible light irradiation without photocatalysts. Dis-C_3N_4 had an improved photodegradation effects due to its improved surface area over bulk-C_3N_4. However, 200-C_3N_4 performs much higher degradation rate even though the surface area was lower (see Figure 9a). As shown in Figure 9a, 200-C_3N_4 was able to completely decoloring MO in 45 min irradiation while dis-C_3N_4 decolored 98% MO in 120 min. Among the g-C_3N_4 PCs, 200-C_3N_4 displayed the highest photodegrading activity, suggesting the photocatalysis activity was related to the stop bands of the g-C_3N_4 PCs. HPLC results in Figure S11 in the Supporting Information supported the improved photocatalysis activity of 200-C_3N_4 and indicated that the major degradation process could be the demethylated (*N*-methyl) route in the first step.

Figure 9c concluded the two major mechanisms how the stop band in g-C_3N_4 led to enhanced photocatalytic activity. Firstly, the stop band could reduce the radiative recombination via decreasing photonic density of states when the stop band overlapped with the emission curve. Secondly, the stop band could increase light absorption via slow light effects when the red-edge of the stop band overlapped with the photocatalytic absorption range of g-C_3N_4. (The light in a PC travels with very low group velocity near the photonic stop-band edges due to multiple back scattering and the forming of stand waving, referred to as slow light.[27] Such slow photon effects can increase the effective optical path length at the red edge of stop-band, promoting light absorption of the photocatalytic PCs.[27–30]) As these two effects referred to different wavelength of the stop band (hence different incidence angle of the same PC g-C_3N_4), Figure 9c indicated the incident angle region for 200-C_3N_4 which could lead to PL depression or slow light effects. The stop bands based on normal incidence for the g-C_3N_4 PCs from 180-C_3N_4 to 260-C_3N_4 were 442, 480, 510, 568, and 599 nm, respectively. According to the reported works, the position of the slow light was located in the long wavelength edge of the stop band.[27–32] Taking into account the random distribution of incident angle to the g-C_3N_4 PCs in the suspension, we calculated the incident-angle-dependent diffraction maxima of the 200-C_3N_4 (see Figure 9c). According to the modified Bragg's law (see Equation (2) in Section 4), the stop band position would shift to shorter wavelength with the increasing incident angle. As the stop band blue-shifts with the increasing incident angle, the long wavelength edge of the stop band (about 60 nm from the diffraction maxima) overlapped with the irradiation light and the absorption band of g-C_3N_4, leading to the enhanced absorption via slow light effects and the improved photocatalysis. It is needed to be pointed out that there could be a third mechanism for the photocatalysis enhancement:

Adv. Funct. Mater. **2016**,
DOI: 10.1002/adfm.201600894

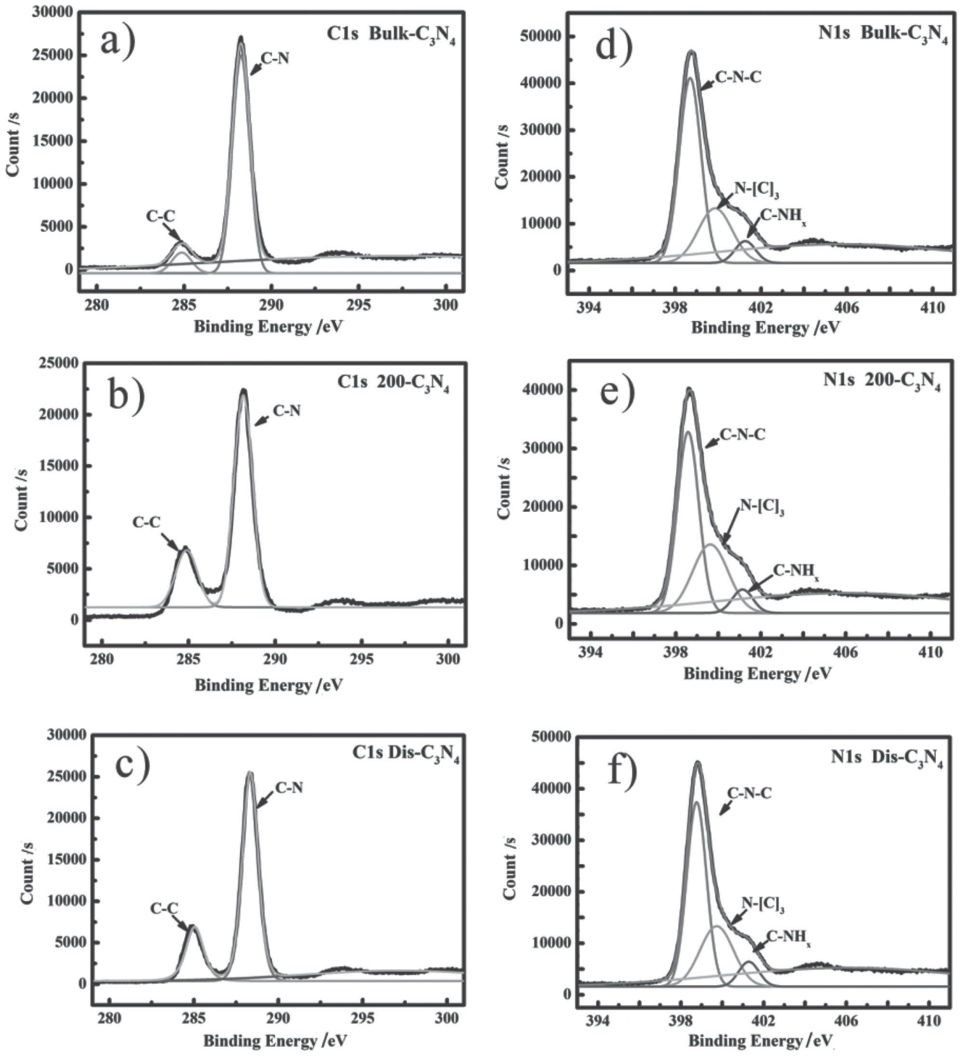

Figure 5. C1s and N1s XPS spectra of bulk-C_3N_4, 200-C_3N_4 and dis-C_3N_4, respectively.

stronger reflections by the photonic structure from the back of the photocatalysis. Ge and co-workers reported the synergetic enhancement of meso-C_3N_4 nanorods with PC films as support substrates.[33]

In HER measurement, 3 wt% Pt was loaded onto all of the g-C_3N_4 samples to increase activity via forming a metal-semiconductor heterojunction (see Figure S12 in the Supporting Information).[1b] Figure S13 in the Supporting

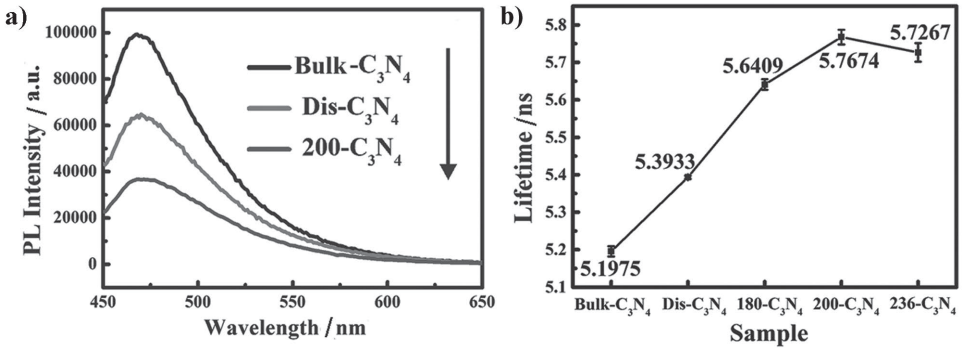

Figure 6. a) PL spectra under 420 nm excitation and b) the measured values of lifetime by time-resolved PL spectra monitored at 470 nm under 406.2 nm excitation at 298 K for bulk-C_3N_4, dis-C_3N_4, and g-C_3N_4 PCs powder suspension in water.

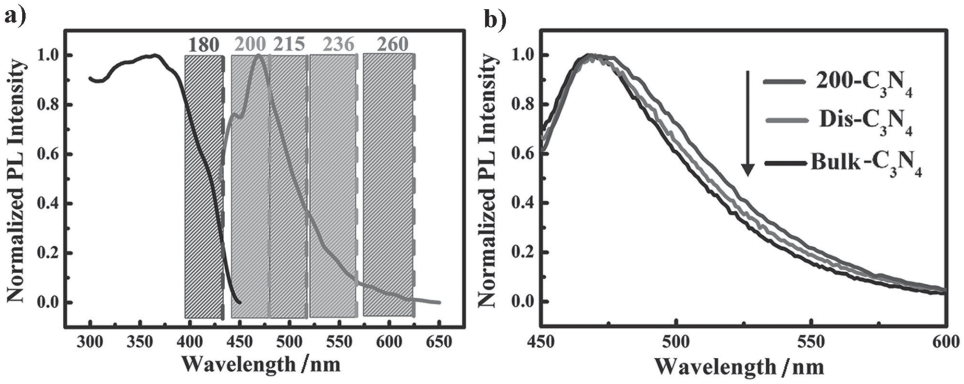

Figure 7. a) Normalized excitation and emission spectra under 420 nm (bleft and right line traces, respectively) of bulk-C_3N_4 suspension, with the stop band maxima of the 180-C_3N_4, 200-C_3N_4, 215-C_3N_4, 230-C_3N_4, and 260-C_3N_4, based on normal incidence (dashed lines) and 0–35 °C (one half of the crystal plane angle of PC {111} planes) incidence (hatching regions). b) Normalized PL spectra under 420 nm excitation for bulk-C_3N_4, dis-C_3N_4, and 200-C_3N_4 powder suspension in water.

Information demonstrates that the Pt nanoparticles with diameters about 5–10 nm were well-dispersed on the wall of the 200-C_3N_4. As shown in Figure 9b, the HER of dis-C_3N_4 was 1260 μmol g^{-1} h^{-1} with an enhancement factor of 5.6 which was close to its specific surface area enhancement from bulk-C_3N_4 (6.1 times). The HER of 200-C_3N_4 was 1979 μmol g^{-1} h^{-1}, with an enhancement factor of 8.82 when compared with bulk-C_3N_4 (224.4 μmol g^{-1} h^{-1}), while the surface area of 200-C_3N_4 was only 5.29 times larger than the bulk-C_3N_4. Therefore, the H_2 evolution enhancement was further attributed to slow photon effects, PL depression and multiple scatterings of the g-C_3N_4 PCs. The 200-C_3N_4 was one of the most effective macropore regulated g-C_3N_4 without changing the band gap and crystallization of g-C_3N_4 (see Table S2 in the Supporting Information). In addition, the HER of 200-C_3N_4 was stable during through 12 h experiment. The chemical and morphology stability of 200-C_3N_4 were evidenced by FTIR (Figure S15, Supporting Information), XPS (Figure S16, Supporting Information), and SEM (Figure S5b,c, Supporting Information) characterizations after the hydrogen evolution. 200-C_3N_4 without grinding also had higher HER than bulk-C_3N_4 powder even though the area for receiving light was much less than that of the powder form (see Figure S14 in the Supporting Information). Higher efficiency could be obtained by doping, amorphization and introducing mesoporous structure.

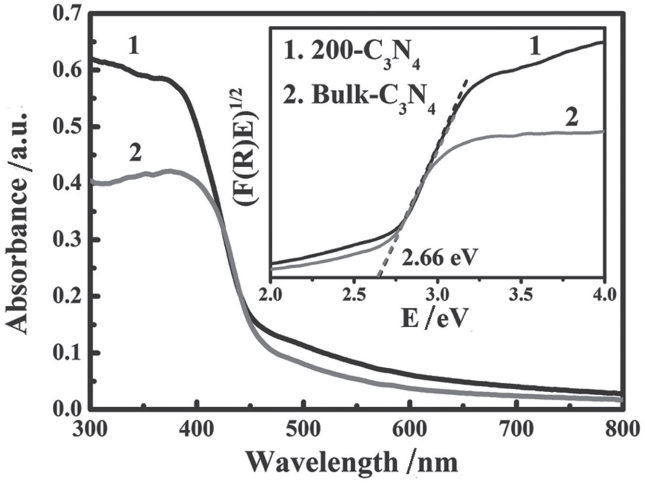

Figure 8. UV–vis diffuse spectrum of 200-C_3N_4 and bulk-C_3N_4 powder. Inset: the corresponding Tauc plots.

3. Conclusion

In summary, freestanding macroscopic g-C_3N_4 PCs were obtained by highly ordered, crack-free colloidal crystal templating. The g-C_3N_4 PCs exhibited enhanced photodegradation and hydrogen evolution activity under visible light irradiation, as a result of the combination of slow photon effects, multiple scatterings, hierarchical porous structure and quenched radiative recombination, with a hydrogen evolution rate of 1979 μmol g^{-1} h under $\lambda > 420$ nm irradiation, 8.82 times as much as that of bulk g-C_3N_4. In addition to the promising application of g-C_3N_4 PCs as a photocatalyst for water splitting, we anticipate that this work provides a facile and low-cost method for incorporation of freestanding PC materials to a wide variety of devices.

4. Experimental Section

Synthesis of Silica PCs: Monodispersed silica microspheres with diameters of 180–260 nm were synthesized via Stöber method.[44] Briefly, tetraethyl orthosilicate (TEOS, 1.0–2.5 g) was dissolved in ethanol (36 mL) at 25 °C, followed by slowly adding the mixture of ammonia (1.8 g) and deionized water (1.8 g). The mixture was kept stirring at 25 °C for 12 h. The diameter of the silica microspheres could be adjusted by varying the amount of TEOS and the temperature. After that, monodisperse silica microspheres were obtained after centrifugation and dispersion in water for several times to remove the residues. Afterward, the obtained silica spheres, which dispersed in water with a concentration of 5 wt%, were allotted into 10 mL vials. The silica PCs self-assembled on the wall of the vials at 60 °C with a relative humidity of 65% for ≈48 h, with little sediment at the bottom.

Synthesis of Disordered Silica Aggregate: Multi-dispersed silica microspheres with average diameter of 120 nm were synthesized as follows: 17 g tetraethyl was orthosilicate dissolved in 360 mL ethanol at 25 °C, followed by pouring in the mixture of 18 g ammonia and 18 g

Adv. Funct. Mater. 2016,
DOI: 10.1002/adfm.201600894

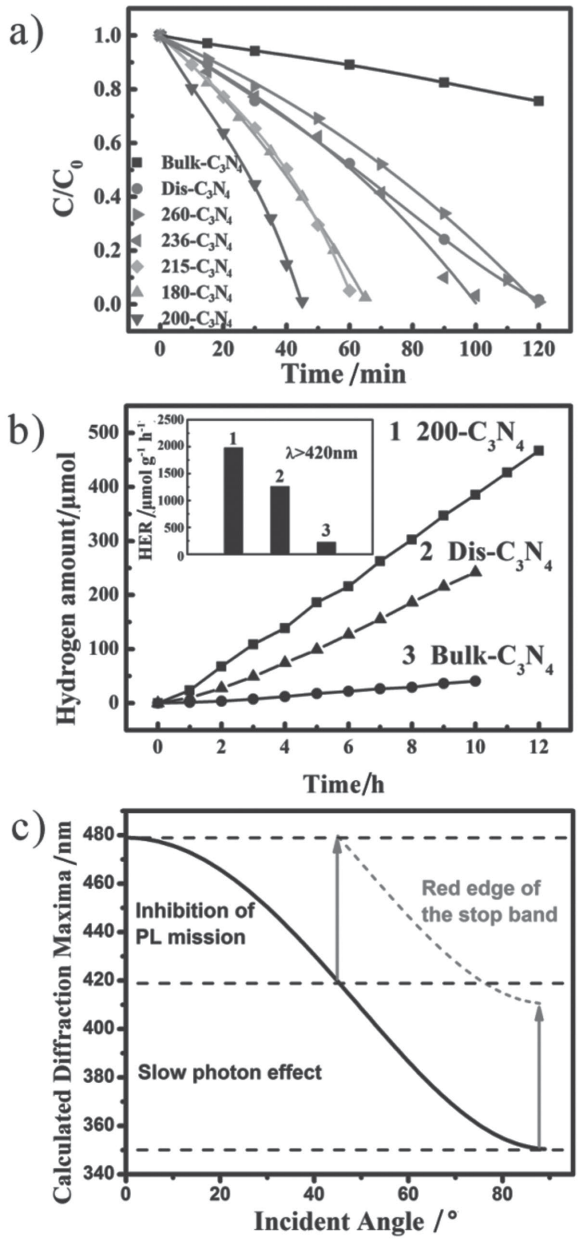

Figure 9. a) Concentration changes of MO as a function of irradiation time with different photocatalyst samples as powder under visible light irradiation (λ > 420 nm). C_0 = 20 mg L^{-1}. b) Hydrogen evolution of 200-C_3N_4, dis-C_3N_4, and bulk-C_3N_4 powder under visible light irradiation (λ > 420 nm) with 3 wt% Pt, and triethanolamine as a hole scavenger. c) Calculated incident-angle-dependent diffraction maxima of the 200-C_3N_4 (black solid line) and the red edge of the stop band within the absorption region of g-C_3N_4 (upper short dashed line).

deionized water. The mixture was kept stirring at 25 °C for 12 h. The purification and assembling method were the same with the silica PCs.

Synthesis of g-C_3N_4 PCs and Disordered g-C_3N_4: Firstly, DCDA (0.3 g) was mixed with silica PCs (0.5 g) or disordered silica aggregate, and calcined in N_2 at 520 °C with a ramp of 2 °C min^{-1} for 2 h. Afterward, the product was further heated to 550 °C with a ramp of 4 °C min^{-1} and kept at 550 °C min^{-1} for another 2 h. The as-obtained product was etched using 4 M NH_4HF_2 solvent for 72 h to remove the silica templates completely, washed with DI water three times and dried under ambient conditions. The yield based on carbon atom was about 68.5 wt%.

Synthesis of Bulk g-C_3N_4 PCs: For comparison, bulk g-C_3N_4 without PC structure was prepared by direct annealing DCDA in N_2 with the same treatments with g-C_3N_4 PCs.

Preparation of Photoelectrode: Firstly, powdered photocatalysts were transformed into slurry (5 mg mL^{-1} in N,N-dimethyformamide, with one drop of 0.25% Nafion) under sonication. The slurry was then dip-coated onto a clean indium-tin oxide (ITO) conductor glass with a controlled area of 0.25 cm^2 to form a film electrode. Finally the photoelectrode was dried and heated at 200 °C in air.

Characterization: Powder XRD measurements were performed on Rigaku Co SmartLab. XPS data were obtained on Thermo ESCALAB 250 instrument with a monochromatized AlKα line source (200 W). All binding energies were referenced to the C1s peak at 284.6 eV. Elemental analyses for C and N were carried out in an Elementar Vario EL elemental analyzer. Reflectance spectra were measured by Ocean optics USB-2000+ fiber spectrophotometer coupled with a tungsten halogen light source and a fiber optic reflection probe. The UV–vis DRS for g-C_3N_4 and UV–vis absorption spectra for MO solutions were measured on Shimadzu UV-3600. Nitrogen adsorption–desorption isotherms were collected at 77 K using Micromeritics ASAP 2020 M. SEM images were taken on Hitachi S-4800 field-emission microscope. PL spectra were recorded on an Edinburgh FLS 980 spectrophotometer. Electrochemical measurements were conducted with a CHI Electrochemical System. HPLC measurements were carried out on a Hewlett Packard HP1100 high performance liquid chromatography with acetonitrile: 0.01 mol L^{-1} ammonium acetate aqueous solution = 3:7 V/V as mobile phase at speed of 0.8 mL min^{-1}. Transmission electron microscope (TEM) images were taken on JEOL JEM-2100F field-emission microscope. FTIR measurement was carried out on a Nicolet-Nexus 670 infrared spectrophotometer.

Photocurrent Analysis: Electrochemical measurements were performed on a CHI Electrochemical System with a conventional three electrode cell in 0.2 M Na_2SO_4 aqueous solution with 0.1 V bias potential, where a Pt plate and an Ag/AgCl electrode (3 M KCl for photocurrent measurement and saturated KCl for impedance measurement) were used as counter electrode and reference electrode, respectively. Before each measurement, the electrolyte solution was well purged with nitrogen prior to the measurements. The visible light was generated by a 300 W xenon lamp (Microsolar 300) with appropriate long-pass cut-off filters.

Photocatalytic Photodegradation Test: The photodegradation activities were evaluated by the decomposition of MO under visible light irradiation (λ > 420 nm). Visible irradiation was obtained from a 300 W xenon lamp (Microsolar 300, PerfectLight, Beijing) with a 420 nm cut-off filter. Before irradiation, powdered photocatalyst (35 mg) were magnetically stirred in MO aqueous solution (35 mL, 20 mg L^{-1}) for 4 h in dark for adsorption equilibrium. At certain time intervals, aliquots (3 mL) were sampled and centrifuged to remove the particles. The concentration of MO was analyzed by recording the UV–vis absorption maxima which could blue-shift from 466 to 452 nm during the degradation.

Photocatalytic H_2 Evolution Test: Photocatalytic water splitting was carried out in a Pyrex top-irradiation reaction vessel connected to a glass closed gas circulation system. H_2 evolution was performed by dispersing 20 mg of powdered photocatalyst in an aqueous solution (100 mL) containing triethanolamine (10 vol%) as sacrificial electron donor. 3 wt% Pt was photodeposited onto the catalyst using $H_2PtCl_6{\cdot}6H_2O$ dissolved in the reactant solution. The reaction solution was evacuated several times to remove air completely prior to irradiation under a 300 W Xeon-lamp with a 420 nm cut-off filter. The temperature of the reaction solution was maintained at room temperature by the cooling of circulating water during the reaction. The evolved gases were analyzed by gas chromatography (7820A, Agilent) equipped with a thermal conductive detector and a 5 Å molecular sieve column, using Argon as the carrier gas.

Calculation of the Incident-Angle-Dependent Diffraction Maxima: The correlation between the stop band, spherical diameter, and incidence angle could be summarized by following equation

$$\lambda_{max} = 2\sqrt{\frac{2}{3}}D\sqrt{n^2_{g\text{-}C_3N_4}f + n^2_{water}(1-f) - \sin^2\theta} \quad (2)$$

where λ_{max} is the wavelength of stop band (diffraction maxima), D is the spherical diameter of the inverse opal (taken the same as the silica PCs due to the hard templating), f is the g-C_3N_4 phase volume percentage (0.26), θ is the incidence angle, $n_{g\text{-}C_3N_4}$ and n_{water} are the refractive index of g-C_3N_4 (1.80) and water (1.33) respectively.

Supporting Information

Supporting Information is available from the Wiley Online Library or from the author.

Acknowledgements

This work was supported by the National Natural Science Foundation of China (Grant Nos. 51233008, 51503229) and the Natural Science Foundations of Guangdong Province of China (2015A030310212). The authors are very grateful for the great supports from Yanan Fan and Weiqing Zhang from School of Chemistry and Chemical Engineering, Sun Yat-sen University.

Received: February 19, 2016
Revised: March 29, 2016
Published online:

[1] a) S. Cao, J. Low, J. Yu, M. Jaroniec, *Adv. Mater.* **2015**, *27*, 2150; b) X. H. Li, M. Antonietti, *Chem. Soc. Rev.* **2013**, *42*, 6593.
[2] X. Wang, K. Maeda, A. Thomas, K. Takanabe, G. Xin, J. M. Carlsson, K. Domen, M. Antonietti, *Nat. Mater.* **2009**, *8*, 76.
[3] Q. Han, B. Wang, Y. Zhao, C. Hu, L. Qu, *Angew. Chem. Int. Ed.* **2015**, *54*, 11433.
[4] K. Schwinghammer, B. Tuffy, M. B. Mesch, E. Wirnhier, C. Martineau, F. Taulelle, W. Schnick, J. Senker, B. V. Lotsch, *Angew. Chem. Int. Ed.* **2013**, *52*, 2435.
[5] J. Zhang, G. Zhang, X. Chen, S. Lin, L. Möhlmann, G. Dołęga, G. Lipner, M. Antonietti, S. Blechert, X. Wang, *Angew. Chem. Int. Ed.* **2012**, *124*, 3237.
[6] a) Y. Cui, Z. Ding, X. Fu, X. Wang, *Angew. Chem. Int. Ed.* **2012**, *51*, 11814; b) Y. S. Jun, J. Park, S. U. Lee, A. Thomas, W. H. Hong, G. D. Stucky, *Angew. Chem. Int. Ed.* **2013**, *52*, 11083; c) Y. S. Jun, E. Z. Lee, X. Wang, W. H. Hong, G. D. Stucky, A. Thomas, *Adv. Funct. Mater.* **2013**, *23*, 3661.
[7] D. J. Martin, K. Qiu, S. A. Shevlin, A. D. Handoko, X. Chen, Z. Guo, J. Tang, *Angew. Chem. Int. Ed.* **2014**, *53*, 9240.
[8] J. Zhang, J. Sun, K. Maeda, K. Domen, P. Liu, M. Antonietti, X. Fua, X. Wang, *Energy Environ. Sci.* **2011**, *4*, 675.
[9] K. Schwinghammer, B. Tuffy, M. B. Mesch, E. Wirnhier, C. Martineau, F. Taulelle, W. Schnick, J. Senker, B. V. Lotsch, *Angew. Chem. Int. Ed.* **2013**, *52*, 2435.
[10] Y. Kang, Y. Yang, L. C. Yin, X. Kang, G. Liu, H. M. Cheng, *Adv. Mater.* **2015**, *27*, 4572.
[11] a) P. Niu, L. Zhang, G. Liu, H. M. Cheng, *Adv. Funct. Mater.* **2012**, *22*, 4763; b) S. Yang, Y. Gong, J. Zhang, L. Zhan, L. Ma, Z. Fang, R. Vajtai, X. Wang, P. M. Ajayan, *Adv. Mater.* **2013**, *25*, 2452; c) J. Zhang, M. Zhang, C. Yang, X. Wang, *Adv. Mater.* **2014**, *26*, 4121.
[12] Q. Liang, Z. Li, Z. H. Huang, F. Kang, Q. H. Yang, *Adv. Funct. Mater.* **2015**, *25*, 6885.
[13] C. A. Caputo, M. A. Gross, V. W. Lau, C. Cavazza, B. V. Lotsch, E. Reisner, *Angew. Chem. Int. Ed.* **2014**, *53*, 11538.
[14] Y. Wang, R. Shi, J. Lin, Y. Zhu, *Energy Environ. Sci.* **2011**, *4*, 2922.
[15] J. Zhang, M. Zhang, R. Q. Sun, X. Wang, *Angew. Chem. Int. Ed.* **2012**, *124*, 10292.
[16] X. Wang, K. Maeda, X. Chen, K. Takanabe, K. Domen, Y. Hou, X. Fu, M. Antonietti, *J. Am. Chem. Soc.* **2009**, *131*, 1680.
[17] J. Sun, J. Zhang, M. Zhang, M. Antonietti, X. Fu, X. Wang, *Nat. Commun.* **2012**, *3*, 1139.
[18] D. Zheng, C. Pang, Y. Liu, X. Wang, *Chem. Commun.* **2015**, *51*, 9706.
[19] Q. Liang, Z. Li, X. Yu, Z. H. Huang, F. Kang, Q. H. Yang, *Adv. Mater.* **2015**, *27*, 4634.
[20] K. Kailasam, J. D. Epping, A. Thomas, S. Losseb, H. Jungeb, *Energy Environ. Sci.* **2011**, *4*, 4668.
[21] J. Zhang, F. Guo, X. Wang, *Adv. Funct. Mater.* **2013**, *23*, 3008.
[22] S. John, *Phys. Rev. Lett.* **1987**, *58*, 2486.
[23] E. Yablonovitch, *Phys. Rev. Lett.* **1987**, *58*, 2089.
[24] A. C. Arsenault, T. J. Clark, G. V. Freymann, L. Cademartiri, R. Sspienza, J. Bertolotti, E. Vekris, S. Wong, V. Kitaev, I. Manners, R. Z. Wang, S. John, D. Wiersma, G. A. Ozin, *Nat. Mater.* **2006**, *5*, 179.
[25] C. Blum, A. P. Mosk, I. S. Nikolaev, V. Subramaniam, W. L. Vos, *Small* **2008**, *4*, 492.
[26] M. Li, F. He, Q. Liao, J. Liu, L. Xu, L. Jiang, Y. Song, S. Wang, D. Zhu, *Angew. Chem. Int. Ed.* **2008**, *47*, 7258.
[27] T. Baba, *Nat. Photon.* **2008**, *2*, 465.
[28] A. Mihi, C. Zhang, P. V. Braun, *Angew. Chem. Int. Ed.* **2011**, *50*, 5712.
[29] S. Nishimura, N. Abrams, B. A. Lewis, L. I. Halaoui, T. E. Mallouk, K. D. Benkstein, J. Lagemaat, A. J. Frank, *J. Am. Chem. Soc.* **2003**, *125*, 6306.
[30] L. Liu, S. K. Karuturi, L. T. Su, A. I. Y. Tok, *Energy Environ. Sci.* **2011**, *4*, 209.
[31] a) X. Zhang, Y. Liu, S. T. Lee, S. Yang, Z. Kang, *Energy Environ. Sci.* **2014**, *7*, 1409; b) J. Liu, G. Liu, M. Li, W. Shen, Z. Liu, J. Wang, J. Zhao, L. Jiang, Y. Song, *Energy Environ. Sci.* **2010**, *3*, 1503.
[32] X. Chen, J. Ye, S. Ouyang, T. Kako, Z. Li, Z. Zou, *ACS Nano* **2011**, *5*, 4310.
[33] F. Pang, Y. Jiang, Y. Zhang, M. He, J. Ge, *J. Mater. Chem. A* **2015**, *3*, 21439.
[34] B. T. Holland, C. F. Blanford, A. Stein, *Science* **1998**, *281*, 538.
[35] Y. Xia, B. Gates, Y. Yin, Y. Lu, *Adv. Mater.* **2000**, *12*, 693.
[36] P. Jiang, M. J. McFarland, *J. Am. Chem. Soc.* **2004**, *126*, 13778.
[37] S. Wong, V. Kitaev, G. A. Ozin, *J. Am. Chem. Soc.* **2003**, *125*, 15589.
[38] Z. Zhou, X. S. Zhao, *Langmuir* **2005**, *21*, 4717.
[39] S. Guldin, S. Hüttner, M. Kolle, M. E. Welland, P. M. Buschbaum, R. H. Friend, U. Steiner, N. Tétreault, *Nano Lett.* **2010**, *10*, 2303.
[40] M. Barth, A. Gruber, F. Cichos, *Phys. Rev. B* **2005**, *72*, 085129.
[41] E. V. Schwoob, C. Weisbuch, H. Benisty, S. Olivier, S. Varoutsis, I. R. Philip, R. Houdré, C. J. M. Smith, *Phys. Rev. Lett.* **2005**, *95*, 183901.
[42] E. Bovero, F. C. J. M. V. Veggel, *J. Am. Chem. Soc.* **2008**, *130*, 15374.
[43] P. Atkins, R. Friedman, *Molecular Quantum Mechanics*, 5th ed., Oxford University Press, Oxford, UK, **2011**, p. 202.
[44] W. Stöber, A. Fink, E. Bohn, *J. Colloid Interface Sci.* **1968**, *26*, 62.